Acta Materialia 241 (2022) 118408

Contents lists available at ScienceDirect

Acta Materialia

journal homepage: www.elsevier.com/locate/actamat

Full length article

Clarifying the mitigation effect of proton irradiation on the intergranular oxidation of 316L stainless steel in high temperature water

Shengkai Wang[a], Shihao Zhang[a], Jiayu Xie[a], Xingyu Feng[a], Miao Song[b], Gary S. Was[c], Wenjun Kuang[a,*]

[a] Center for Advancing Materials Performance from the Nanoscale (CAMP-Nano), State Key Laboratory for Mechanical Behavior of Materials, Xi'an Jiaotong University, Xi'an 710049, PR China.
[b] School of Nuclear Science and Engineering, Shanghai Jiao Tong University, Shanghai 200240, PR China
[c] Department of Nuclear Engineering and Radiological Sciences, University of Michigan, Ann Arbor, MI 48109, USA

ARTICLE INFO

Article history:
Received 17 June 2022
Revised 24 August 2022
Accepted 29 September 2022
Available online 1 October 2022

Keywords:
Stainless steel
Radiation-induced segregation
Intergranular oxidation
Si-enriched oxide
Scanning transmission electron microscopy

ABSTRACT

The role of proton irradiation in the intergranular oxidation of 316L stainless steel after long-term immersion in simulated PWR primary water was clarified by comparing the microstructural and microchemical features of oxide between the irradiated grain boundary (GB) and its un-irradiated counterpart. As such, the interference from difference in GB structure can be ruled out. Surprisingly, the results reveal that the intergranular oxide penetration in the irradiated region is shallower than that in the un-irradiated region. It is found that Si segregated at the irradiated GB diffuses outwards preferentially and gets oxidized due to its high diffusivity and affinity to oxygen. The Si-enriched oxide in the intergranular oxide tip of irradiated GB can act as a temporary diffusion barrier for oxygen, although it tends to dissolve near the sample surface. Meanwhile, the efficiency of elements (especially Cr) transport along irradiated GB to the oxidation front is promoted mainly due to the vacancies created by preferential diffusion of Si, resulting in higher Cr content at the intergranular oxide tip. The combination of Si and Cr enrichments in the intergranular oxide tip can enhance the resistance to oxidation and eventually leads to a lower oxidation rate for the irradiated GB. For the first time, our study determines that irradiation can enhance the intergranular oxidation resistance of stainless steel after long-term immersion in simulated PWR primary water when the sample is not stressed.

1. Introduction

Austenitic stainless steels have been widely used as core internals in light water reactors (LWRs) due to the high resistance to corrosion and excellent mechanical properties. However, the stainless steels were found to be susceptible to irradiation-assisted stress corrosion cracking (IASCC), which is a major failure mode for reactor internal components [1–5]. IASCC is an environmental degradation mode under the synergistic action of radiation damage, mechanical stress, and corrosive environment [1,5–7]. Understanding IASCC is challenging as multiple factors are involved. Irradiation accelerates stress corrosion cracking (SCC) as it aggravates the corrosiveness of the environment (e.g., water radiolysis), and changes the mechanical properties and corrosion resistance of a material by inducing displacement damage (e.g., dislocation loops, voids et al.) and elemental segregation (i.e., radiation-induced segregation (RIS) and precipitations). Radiolysis of water causes an increase in corrosion potential due to the formation of oxidizing radiolysis products such as H_2O_2 [8,9]. The increase in corrosion potential leads to the dissolution of Cr-enriched inner oxides layer on stainless steel in high temperature water [10–12]. The defect clusters induced by irradiation result in localized heterogeneous deformation in the form of dislocation channels (DCs). The DCs cause stress accumulation at grain boundaries (GBs) and further result in a degradation of protective oxide film [13–15]. However, the role of RIS in corrosion and SCC has not been well understood yet. It should be pointed out that although some works show that highly-irradiated stainless steel is susceptible to intergranular cracking under mechanical loading in an inert environment [6,16], corrosion is still an essential element for the occurrence of IASCC in most cases [17,18]. Actually, the formation of oxide film has been well recognized as a crucial precursor in the process of SCC based on the internal oxidation and slip-dissolution/oxidation mechanisms

---

* Corresponding author.
E-mail address: wjkuang66@gmail.com (W. Kuang).

https://doi.org/10.1016/j.actamat.2022.118408

[19–22]. More importantly, recent results suggest that intergranular oxidation is a crucial precursor for SCC initiation and propagation of the austenitic stainless steels [4,23,24] and nickel base alloys [25–27] in high temperature water. Therefore, intergranular oxidation of irradiated stainless steels in LWRs is a vital step in IASCC. Determining the role of RIS in intergranular oxidation behavior would be critical in understanding IASCC.

Currently, studies on the influences of radiation damage on the corrosion behavior of stainless steel are still very limited. In the case of the general corrosion behavior of irradiated stainless steel, researchers have not yet reached a consensus on the role of radiation damage [28–31]. As to intergranular oxidation, the most relevant radiation damage is RIS which refers to radiation-induced microchemical segregation on GB, such as depletion of Cr, Fe, Mo and enrichment of Si, Ni, P [32,33]. Deng et al. [28] studied the intergranular oxidation behavior of high angle grain boundaries (HAGBs) from the solution annealed (SA), 0.5 and 3 dpa proton-irradiated specimens in simulated pressurized water reactor (PWR) primary water environment with an exposure period of 500 h and found that the degree of oxidation increases with increasing radiation dose due to the enhanced RIS. Fukumura et al. [34] also found the GB oxidation depth of neutron-irradiated stainless steels, after service in a PWR water environment with an immersion time of 1149 h, increased with increasing dose (3 dpa, 19 dpa and 73 dpa). Boisson et al. [29] performed an exposure experiment for 24 h on 1.5 dpa proton-irradiated stainless steel in simulated PWR primary water and pointed out that the intergranular oxide penetration is deeper in the irradiated area (141 ± 2 nm) than in the unirradiated area (42 ± 2 nm). These studies appear to support that irradiation promotes intergranular oxidation due to the radiation-induced Cr depletion at GB. It seems reasonable that lower Cr content at GB would lead to lower corrosion resistance and thus higher susceptibility to SCC. However, the previous work suggests that Cr depletion at GB does not promote SCC in non-irradiated stainless steels in PWR primary water [32]. Other microchemical features induced by irradiation may also play a critical role in the resistance to intergranular oxidation of irradiated stainless steel and should be paid more attention. More importantly, in the previous study of intergranular oxidation behavior, the differences in GB structure that would result in different resistances to RIS [35,36] and intergranular corrosion [37] have not been accounted for, making it impossible to single out the effect of irradiation.

This study aims to determine the effects of the radiation-induced microchemical changes at GB on the intergranular oxidation behavior of stainless steel after long-term immersion in simulated PWR primary water. Proton irradiation, which can penetrate deep enough for studying the intergranular oxidation behavior, will be used as an effective and economic surrogate to simulate the reactor irradiation [38]. The proton-irradiated and non-irradiated regions of the same random high angle grain boundaries (RHABs) were sampled from the cross-section of irradiated surface for microstructure analysis after the exposure test. This enables direct comparative studies of the intergranular oxidation behavior between the irradiated and non-irradiated regions of a single GB. The interference due to the difference in GB structure can be eliminated, which is necessary for singling out the effect of irradiation on intergranular oxidation. In addition, the intergranular oxidation depths were measured on the cross-sections of both irradiated and unirradiated regions to obtain results with statistical significance.

2. Experimental

2.1. Material

The material used in this study is a solution-annealed (SA) 316L stainless steel with a chemical composition listed in Table 1.

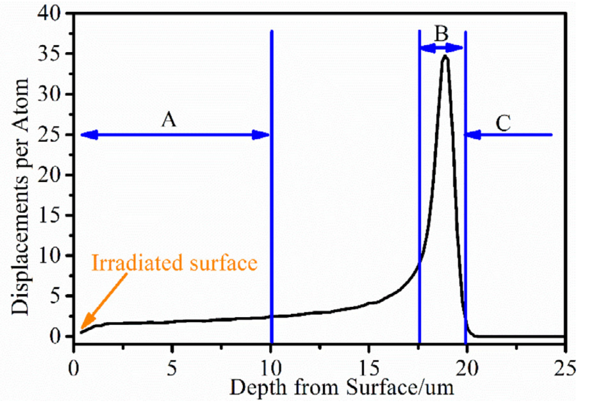

Fig. 1. Damage profile for 316L stainless steels irradiated with 2.0 MeV protons as calculated by SRIM 2013 computer code. A: Uniform damage region (UDR); B: Damage peak region (DPR); C: Non-irradiated region (NIR).

Square bars with a dimension of 10 mm × 2 mm × 2 mm were machined by electrical discharge machining (EDM). The samples were mechanically ground with SiC papers up to 2000 grit and electropolished for 20 s in a solution consisting of 10% perchloric acid and 90% alcohol at -40 °C.

2.2. Proton irradiation

The samples were irradiated using 2 MeV protons at a damage rate around 1×10^{-5} dpa/s at 360 ± 10 °C with a 3 MeV National Electronics Corporation Pelletron accelerator at the Michigan Ion Beam Laboratory (MIBL) at University of Michigan. The SRIM 2013 [39] calculation was adopted with quick Kinchin–Pease option using a displacement energy of 40 eV, and the depth damage profile is given in Fig. 1. About half of the sample surface area was directly irradiated. The damage layer is about 20 μm thick with nearly 10 μm thick uniformly-damaged region (UDR) which has a damage dose of about 2.5 dpa. The proton irradiation procedures were described in more detail elsewhere [40].

2.3. Exposure test

The cross-section of proton-irradiated 316L stainless steel bar was polished for exposure test. During polishing, the irradiated sample was mounted next to another stainless steel square bar to avoid deformation and rounded corners near the edge of cross-section. The sample was wet ground with SiC papers up to 3000 grit, polished with 1.5 μm, 0.5 μm diamond polishing pastes, and finally vibration-polished with 60 nm colloidal silica polishing suspension (3 h) to remove the deformed surface layer. Before the exposure, an FEI Helios Nanolab 600 system equipped with a Nordlys electron back scattering diffraction (EBSD) detector was used to characterize the GB network across the irradiated and non-irradiated regions on the cross section. The EBSD mapping was obtained at a step size of 2 μm with a voltage of 25 kV and a probe current of 5.5 nA. The exposure test was performed in a refreshed 3.6 L autoclave made of 316 stainless steel at a flow rate of 12 L/h in the laboratory of Xi'an Jiao tong University. The sample was exposed to 320 °C, 150 bar high-purity water containing 2.7 ppm H_2 (30 cc H_2/kg H_2O) for 1000 h. Conductivity and dissolved oxygen (DO) of both inlet and outlet water were continuously monitored with Mettler Toledo sensors during the test.

2.4. Analysis of intergranular oxidation

After the exposure test, the sample was removed from the autoclave for further characterization. Only three straight RHABs span-

Table 1
Chemical composition of the 316L stainless steels.

Element	Cr	Ni	Mo	Mn	Si	Co	Ta	S	P	Cu	C	Fe
wt.%	16.20	10.11	2.06	1.58	0.35	0.17	0.017	0.001	0.036	0.37	0.017	Bal.

Table 2
Details about the appropriate three RHABs.

		GB Plane indices		Euler angles: $<\varphi_1, \Phi, \varphi_2>$ in (°)		
GB		Grain 1	Grain 2	Grain 1	Grain 2	MA* in (°)
GB_A	GB_{A1}	$(-1\ -3\ 1)_{\sim 3.21°}$	$(0\ 4\ -3)_{\sim 1.05°}$	(278.8;34.8;11.0)	(45.9;24.4;53.2)	49.9
	GB_{A2}	$(-1\ -3\ 1)_{\sim 2.94°}$	$(0\ 4\ -3)_{\sim 1.22°}$			
GB_B	GB_{B1}	$(0\ -8\ 5)_{\sim 2.62°}$	$(-2\ 2\ -1)_{\sim 1.85°}$	(214.0;51.1;43.4)	(358.6;27.1;31.2)	34.9
	GB_{B2}	$(0\ -8\ 5)_{\sim 2.82°}$	$(-2\ 2\ -1)_{\sim 1.39°}$			
GB_C	GB_{C1}	$(-6\ 7\ -5)_{\sim 1.40°}$	$(1\ 6\ -7)_{\sim 3.07°}$	(16.2;47.8;61.3)	(49.1;38.7;80.6)	49.6
	GB_{C2}	$(-6\ 7\ -5)_{\sim 1.02°}$	$(1\ 6\ -7)_{\sim 2.97°}$			

* MA represents misoriention angle.

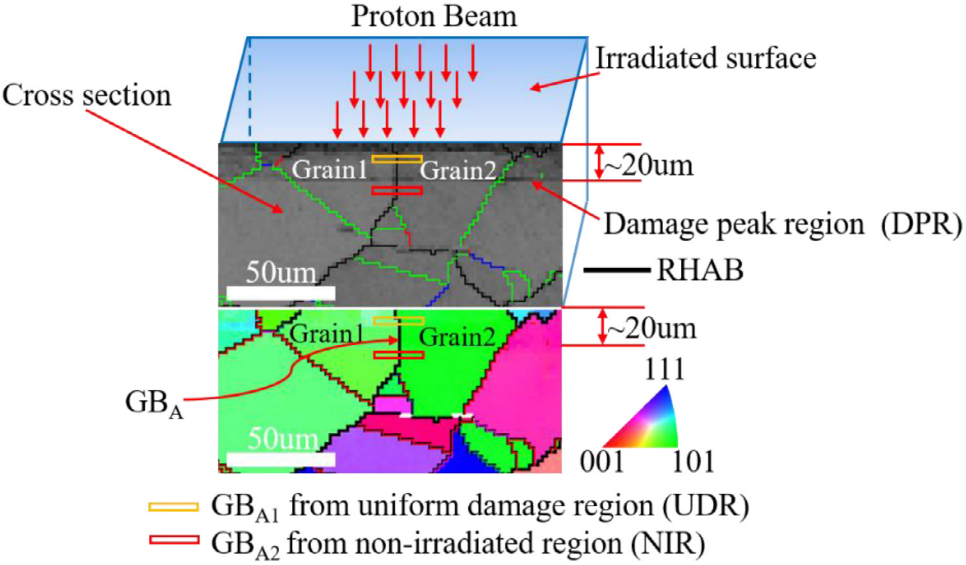

Fig. 2. Schematic of GB_{A1} and GB_{A2} lamellae extraction on the cross section of the irradiated surface.

ning both the irradiated and un-irradiated regions were used for this study and were named GB_A, GB_B and GB_C, respectively. A novel approach was developed in our previous work to determine the GB plane index of a site-specific GB by measuring the Euler angles $<\varphi_1, \Phi, \varphi_2>$ and GB trace angles [41]. The details of these RHABs are summarized in Table 2. Six site-specific transmission electron microscopy (TEM) lamellae (~90 nm thick, polished with 5 kV and 46 pA Ga+ ions) were prepared in a FEI Helios Nanolab 600 Dual Beam focused ion beam (FIB) according to a procedure used before [42]. For each GB, two TEM lamellae were extracted (one from the UDR and the other from non-irradiated region (NIR)) and were designated as GB_{X1} and GB_{X2} (X is A, B or C), respectively. Fig. 2 shows the schematic of GB_{A1} and GB_{A2} lamellae extraction on the cross section of the irradiated surface. The trace of sampled GB is fairly straight, indicating that the indexes of coupled GB planes should be nearly constant along the trace. Microstructure analyses were conducted in a JEOL 2100F TEM under bright field imaging mode along with selected area electron diffraction (SAED) at 200 kV. High-angle annular dark-field (HAADF) images were obtained under scanning TEM (STEM) mode in a JEOL JEM-F200(HR) microscope. The oxide appears darker than the matrix in HAADF images due to its lower average atomic number. The STEM-HAADF images were used to measure the depth of intergranular oxidation with the aid of Image J software. The depths of intergranular oxidation of GB_A, GB_B, and GB_C were marked on the STEM-HAADF images, as shown in Fig. 3. Moreover, elemental distribution was studied using two 100 mm^2 energy dispersive spectroscopy (EDS) detectors equipped in the JEOL JEM-F200(HR). Before the STEM-EDS measurement, the GB was tilted to edge on position to minimize the broadening of the grain boundary. Both STEM-EDS mapping (image resolution: 512 × 512 pixel, dwell time: between 0.5 and 2 ms) and line scanning (step size: between 0.5 and 1 nm, probe size: 5) were conducted to analyze the microchemical features of the intergranular oxide and grain boundary region. It should be noted that the counts of identified elements were used for EDS mapping.

2.5. Measurement of intergranular oxidation depths from cross section

To measure the intergranular oxidation depths from irradiated and unirradiated regions, the corrosion bar was cross sectioned. The oxidized bar was Ni plated to protect the oxide films. Then they were mounted using conductive hot mounting, progressively ground using SiC papers, and then polished using diamond paste and polishing suspension to remove the deformation layer. The cross-section sample was examined across both the irradiated and unirradiated regions using a FEI Verios 460 in back-scattered elec-

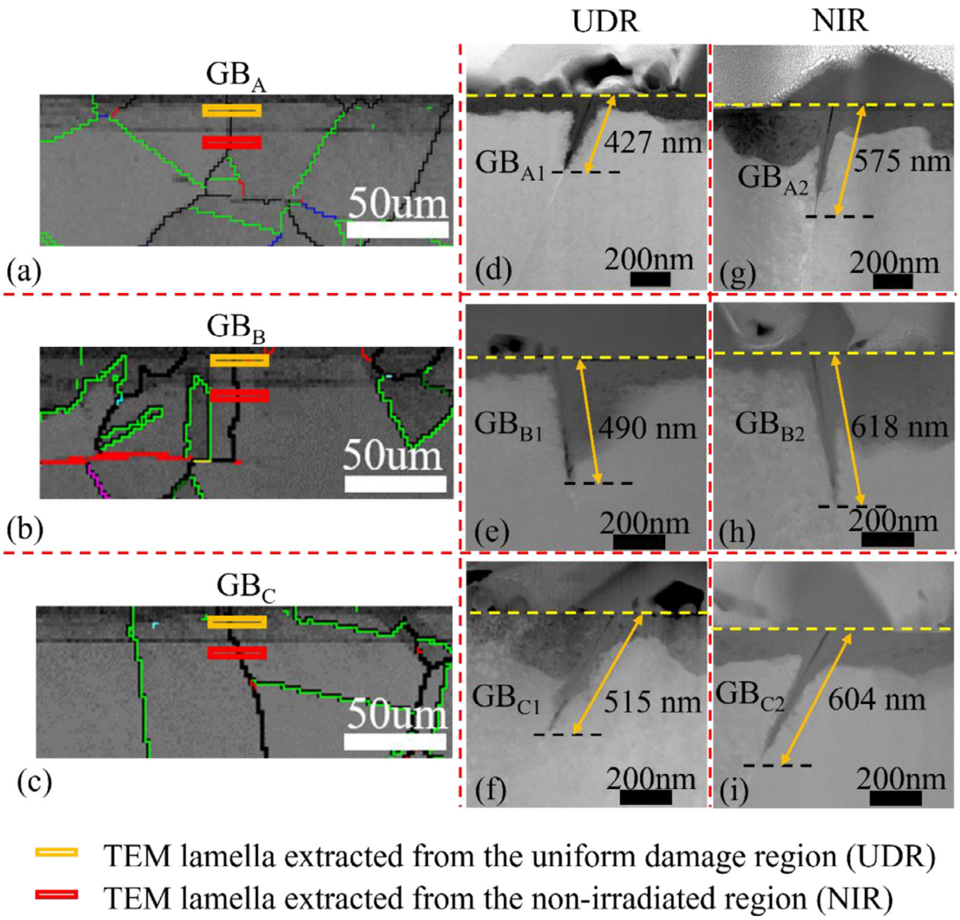

Fig. 3. Characterization of intergranular oxide penetration. (a–c) EBSD band contrast maps show the schematic of GB$_A$, GB$_B$ and GB$_C$ lamellae extraction on the cross section of the irradiated surface, respectively. (d–f) STEM-HAADF images indicate the intergranular oxidation depths of GB$_{A1}$, GB$_{B1}$ and GB$_{C1}$ respectively, which were extricated from UDR. (g–i) STEM-HAADF images indicate the intergranular oxidation depths of GB$_{A2}$, GB$_{B2}$ and GB$_{C2}$ respectively, which were extracted from NIR.

tron (BSE) mode. The beam voltage and probe current size were set to 5 kV and 0.4 nA. It is easy to identify the irradiated and non-irradiated regions as the damage peak region (DPR) can be readily identified in back-scattered electron (BSE) mode. A total of 50 GBs and 38 GBs were measured in the irradiated and unirradiated regions, respectively. The means and standard deviations of the mean were calculated to determine if the intergranular oxidation depths are statistically different between irradiated and unirradiated regions.

3. Results

Fig. 3 shows the traces of sampled GBs on the cross section of the irradiated surface and the STEM-HAADF images of the cross sections of GB$_A$, GB$_B$ and GB$_C$. The traces of these three RHABs on the orthogonal surfaces are fairly straight, indicating the GB structure should be nearly constant along the traces. The sample surfaces, which were specified as outer oxide layer/inner oxide layer interface, were marked on the STEM-HAADF images by straight yellow dashed lines. The depths of intergranular oxidation of GB$_{A1}$, GB$_{B1}$ and GB$_{C1}$, which were extracted from UDR, were marked on Fig. 3d–f, respectively. Meanwhile, the depths of intergranular oxidation of GB$_{A2}$, GB$_{B2}$ and GB$_{C2}$, which were extracted from NIR, were marked on Fig. 3g–i. Quite unexpectedly, the intergranular oxide from UDR is consistently shallower than that from NIR for each GB. The GB plane indices of GB$_A$, GB$_B$ and GB$_C$ were marked on the inverse pole figure (IPF) and the corresponding misorientation angles were also denoted on the IPF (Fig. 4a). The depth of oxidation penetration corresponds to the length of intergranular oxide. Thus, the oxide tip was defined as the point where the oxygen signal decreases significantly in the EDS mapping. The EDS mapping of the enlarged intergranular oxide tip was used to confirm the intergranular oxide tip. Fig. 4b summarizes the depths of intergranular oxidation of these three RHABs. The average intergranular oxide depth of the three GBs in UDR is 477 ± 45 nm while that in NIR is 599 ± 22 nm. In term of percentage, the difference in depths of intergranular oxidation between UDR and NIR ranges from 17% to 35%, which is consistently significant. This conclusion would be compromised by the fact that there is variation in the oxidation depth along a single GB [43]. In order to estimate such variation, two TEM lamellae, which were several microns apart on one GB from irradiated region, were extracted. The results show that the intergranular oxidation depths of these two samples are almost identical (608 nm vs. 612 nm). It appears that the intergranular oxidation depth is quite constant when the GB structure is fixed. To be more statistically significant, measurement of intergranular oxidation depths from cross section was conducted to further confirm the difference in intergranular oxidation depth between UDR and NIR. The results of this measurement will be shown later. The microchemical and microstructural characterizations of GB$_A$, GB$_B$ and GB$_C$ were conducted and the results show very consistent features. Only the results from GB$_A$ were presented here.

Fig. 5 shows the TEM bright field images (under-focus mode) of GB$_{A1}$ and GB$_{A2}$, respectively. The straight yellow dashed lines mark the sample surface, and the solid yellow arrows point to pristine GB$_A$. Radiation-induced voids were observed in the matrix on both

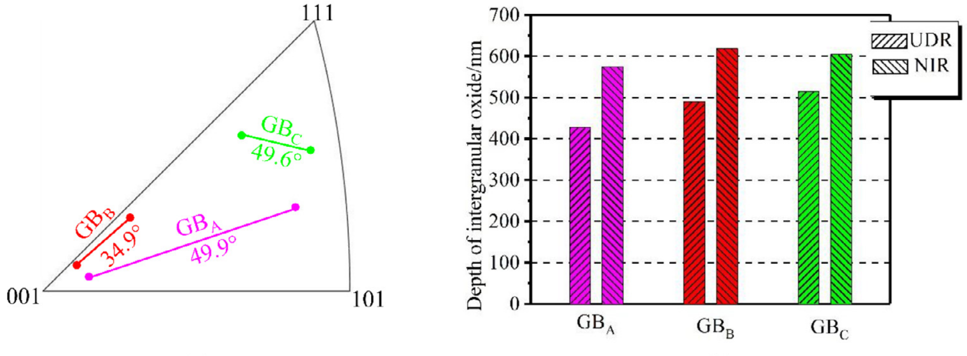

(a) (b)

Fig. 4. (a) GB plane indices of GB$_A$, GB$_B$ and GB$_C$ were marked on the inverse pole figure (IPF) and the corresponding misoriention angles were also denoted on the IPF. (b) Depths of intergranular oxide in UDR and NIR of GB$_A$, GB$_B$ and GB$_C$. (GB plane indices are represented by solid circle and each GB plane pairs belonging to the same GB are connected by solid lines).

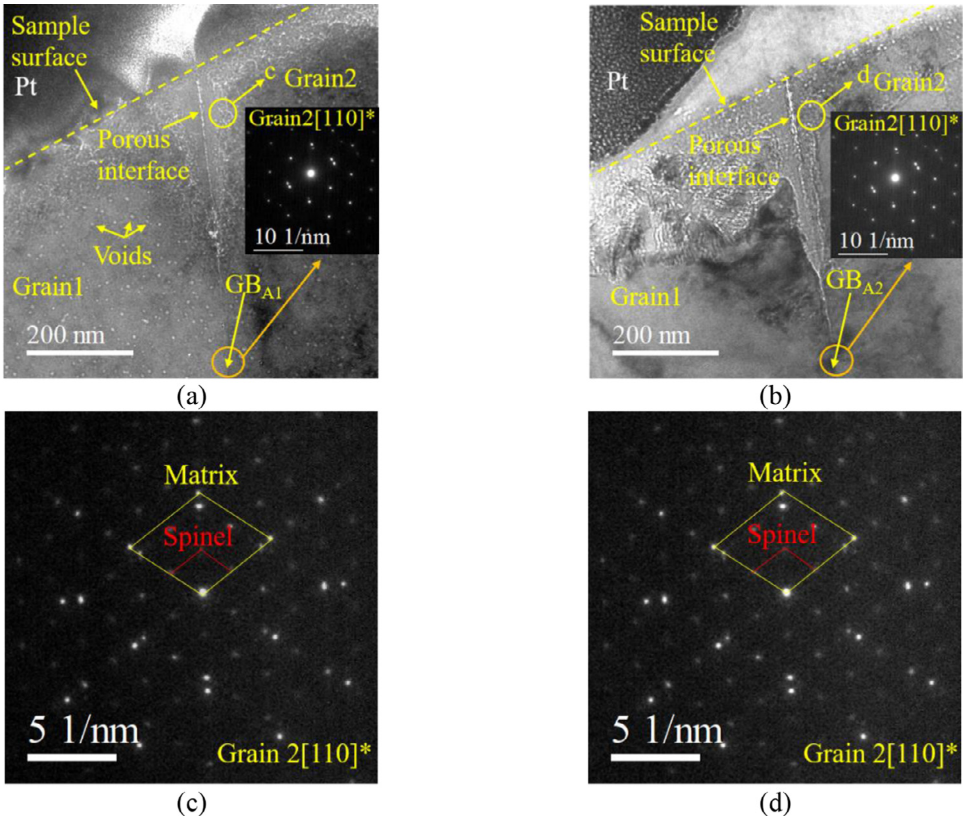

(a) (b) (c) (d)

Fig. 5. Under-focused bright field TEM images of the sampled (a) GB$_{A1}$ and (b) GB$_{A2}$ from UDR and NIR, respectively, (c) SAED pattern of intergranular oxide of GB$_{A1}$ and matrix, (d) SAED pattern of intergranular oxide of GB$_{A2}$ and matrix.

sides of GB$_{A1}$ (as marked in Fig. 5a), while none was observed in the matrix surrounding GB$_{A2}$. Corresponding SAED patterns on the GBs were taken to verify that they have the same GB structure. As shown in the insets in Fig. 5a and b, the SAED patterns taken from the circled areas show the same diffraction patterns. Consistently, the indices of coupled GB planes for GB$_{A1}$ were calculated to be (-1 -3 1)$_{\sim 3.21^{\circ}}$ and (0 4 -3)$_{\sim 1.05^{\circ}}$ and those of GB$_{A2}$ were (-1 -3 1) $_{\sim 2.94^{\circ}}$ and (0 4 -3)$_{\sim 1.22^{\circ}}$, as listed in Table 2. The above results confirm that GB$_{A1}$ and GB$_{A2}$ have almost the same GB structure. Fig. 5c and d show the SAED patterns of intergranular oxide combined with matrix from the two samples. The SAED patterns reveal that the intergranular oxide has a spinel structure that is epitaxial with the matrix, and the structure of intergranular oxide was not changed by proton irradiation. Such intergranular oxide structure is similar to that of neutron-irradiated 316L stainless steel tested in simulated PWR primary environment [44]. It should be noted that porous interfaces within the intergranular oxide near the sample surface were observed along original GB both in UDR and NIR.

Fig. 6a and b show the STEM-HAADF images and EDS mappings of GB$_{A1}$ and GB$_{A2}$. From the HAADF images shown in Fig. 6a and b, the oxide films consist of large outer oxide particles and an inner continuous oxide layer in both UDR and NIR. As shown in Fig. 6, for both UDR and NIR, the intensities of Fe and Ni in the inner continuous oxide layer are lower than those in the matrix while Cr almost maintains similar intensity from matrix to inner oxide. As such, the relative content of Cr ([Cr]/([Fe]+[Cr]+[Ni])) in the inner continuous oxide layer in both UDR and NIR should be much larger than that in the matrix. Thus, the inner continuous oxide

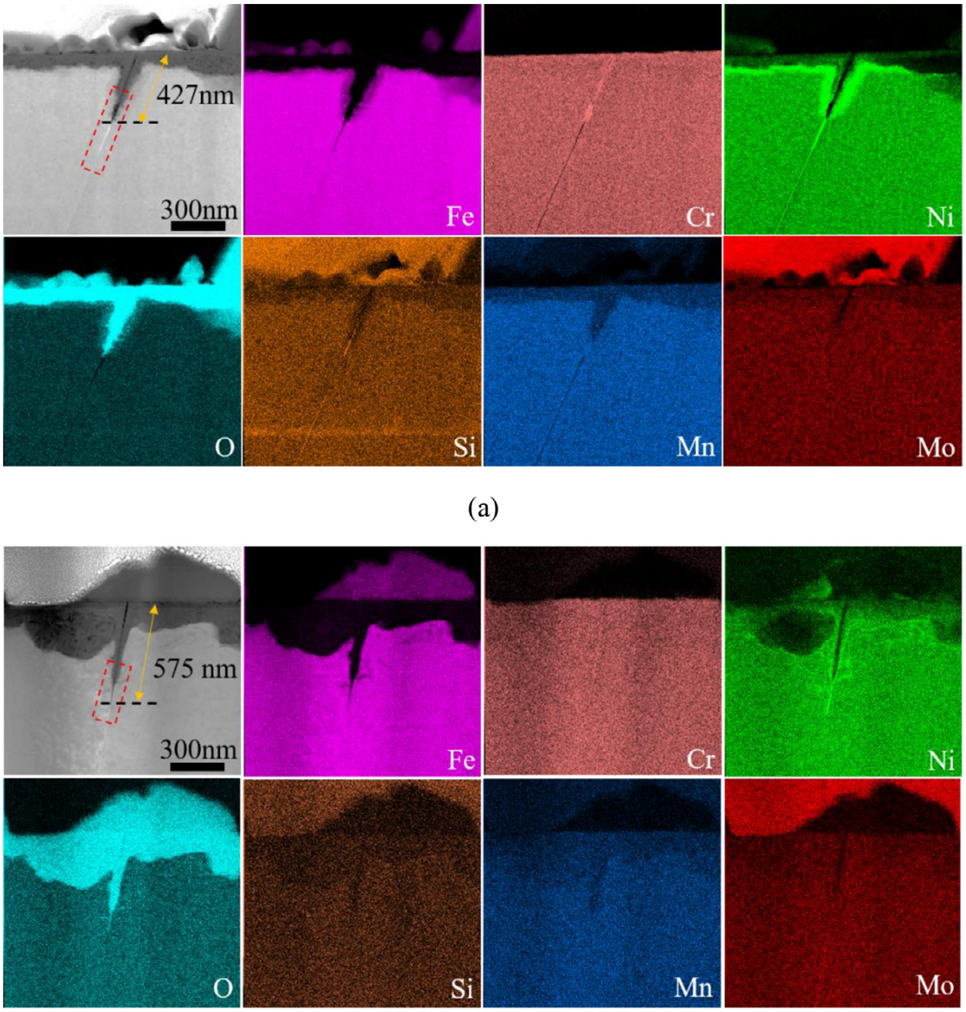

(a)

(b)

Fig. 6. STEM-HAADF images with EDS mappings of (a) GB$_{A1}$ and (b) GB$_{A2}$ from UDR and NIR, respectively.

layer is enriched in Cr. Interestingly, the inner oxide on UDR is more uniform and thinner with a relatively even Ni-enriched transition zone beneath the oxide, as compared to that on NIR. The intergranular oxides in both regions are clearly tapered. The depth of intergranular oxide along GB$_{A1}$ is around 427 nm, while that along GB$_{A2}$ is around 575 nm. A difference in the element composition of the intergranular oxide is noticeable between these two samples. The oxide along GB$_{A1}$ is more enriched in Cr in spite of radiation-induced Cr depletion beyond the oxide. More interestingly, Si segregates at the intergranular oxide tip of GB$_{A1}$, and the degree of enrichment gradually vanishes when approaching the sample surface, suggesting that silicon in oxide near the sample surface was preferentially dissolved into high temperature water. Beyond the intergranular oxide, Si depletion is observed along a GB segment (~250 nm long) in GB$_{A1,}$ although Si was originally enriched due to RIS. Meanwhile, Ni is further enriched in addition to RIS while Fe is depleted. In contrast, GB$_{A2}$ only shows Fe depletion and Ni enrichment beyond the oxide tip. Such chemical segregation results from oxidation and is termed as oxidation affected zone (OAZ) hereafter. It should be noted that the length of OAZ beyond the intergranular oxide along GB$_{A1}$ is larger than that along GB$_{A2}$ (250 nm vs. 94 nm). Beyond the OAZ segment, element segregation due to irradiation is clearly visible along GB$_{A1,}$ which is not observed at GB$_{A2}$. The pristine segment of GB$_{A1}$ is enriched in Ni, Si while depleted in Cr and Mn from the EDS mapping (Fig. 6a).

In fact, the irradiation effect on intergranular oxidation is not only reflected by the variation in oxidation depth, but also more fundamentally by the striking difference in features of intergranular oxide tip and OAZ. To further reveal the differences in microchemistry between GB$_{A1}$ and GB$_{A2}$, the intergranular oxide tips were analyzed with STEM-EDS at higher magnification, as shown in Figs. 7 and 8. Some EDS line profiles were taken as indicated in Figs. 7a and 8a. The intergranular oxide tips of GB$_{A1}$ and GB$_{A2}$ are all enriched in Cr while depleted in Fe and Ni (Figs. 7a and 8a). Most of the intergranular oxides of GB$_{A1}$ and GB$_{A2}$ are depleted in Mn except that in the oxide tips (Figs. 7b–d and 8b and c), indicating that Mn has mostly dissolved into water. Moreover, a remarkable Si enrichment was observed in the intergranular oxide tip of GB$_{A1,}$ while none was found in the intergranular oxide tip of GB$_{A2}$ (Figs. 7a and d and 8a and c). As for the Cr content in the intergranular oxide, it is higher in GB$_{A1}$ than in GB$_{A2}$ (28.0 at.% vs. 20.2 at.%) (Figs. 7a and d and 8a and c). In addition, the composition profiles of Cr across the intergranular oxide of GB$_{A1}$ and GB$_{A2}$ show an "M" shape and an inverted "V" shape (Figs. 7c and 8c), respectively. The results from GB$_{B}$ and GB$_{C}$ also show similar features.

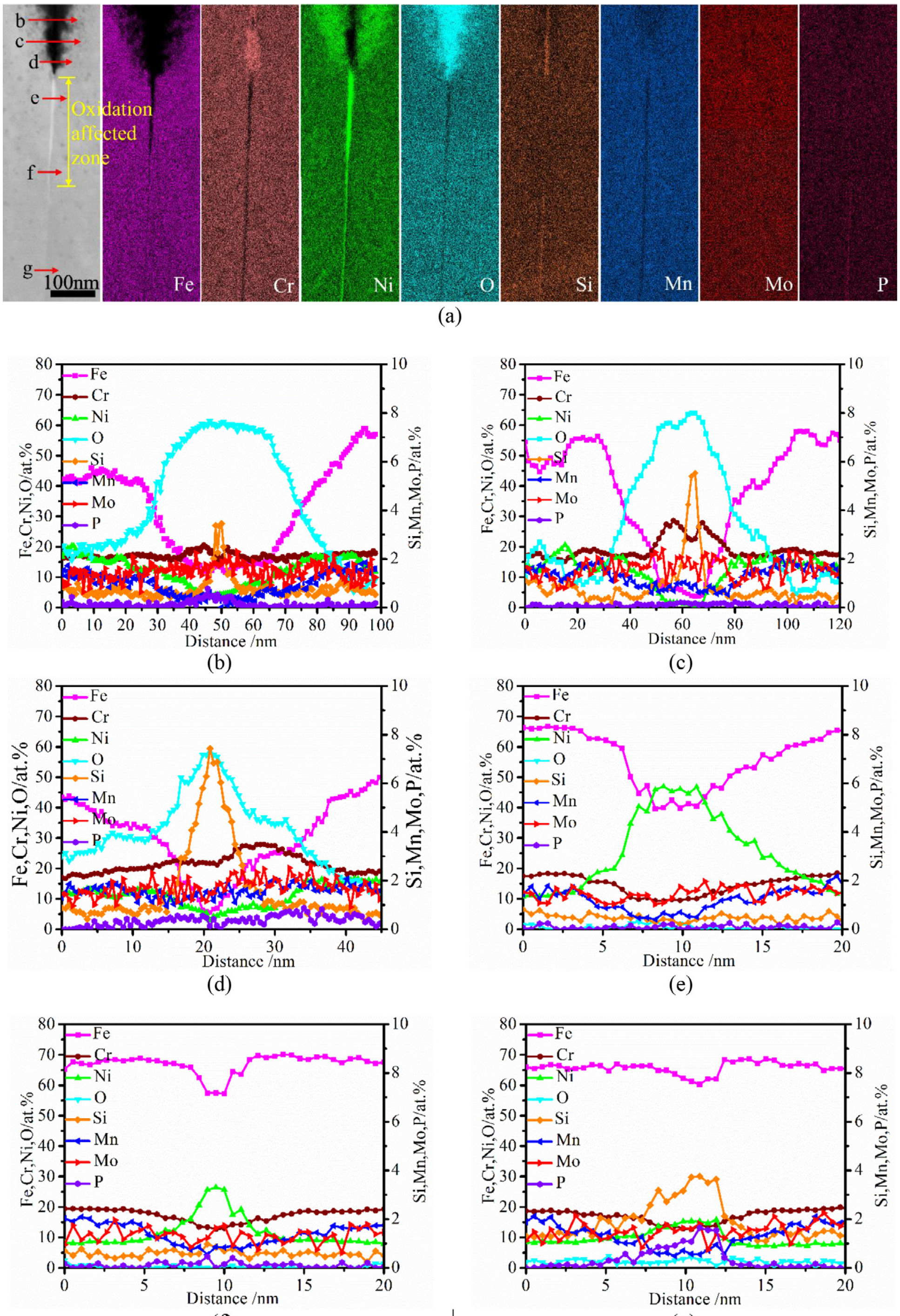

(a)

(b) (c)

(d) (e)

(f) (g)

Fig. 7. (a) STEM-HAADF image and EDS mappings of the enlarged intergranular oxide tip of GB_{A1} (shown in Fig. 4a with red dotted line) in UDR and (b–g) EDS line profiles along the lines in (a).

The EDS line profiles across the intergranular oxide along GB_{A1} are presented in Fig. 7b–d. As shown in Fig. 7b and d, the Si content in the intergranular oxide tip of GB_{A1} decreases gradually from 7.4 at.% (Fig. 7d) to 3.5 at.% (Fig. 7b) when approaching the sample surface. As mentioned above, intergranular oxidation causes additional composition changes in GB just beyond the intergranular oxide. It results in further depletion of Fe, Cr and enrichment of Ni compared to RIS (Fig. 7e–g). The OAZ extends over 250 nm long and 15 nm wide beyond the oxide tip (Fig. 7a and e). More interestingly, the enrichment of Si due to RIS vanished in the OAZ (Fig. 7a, e and f). The RIS of pristine GB in UDR is shown in Fig. 7g. The GB is depleted in Fe, Cr and Mn and enriched in Ni, Si, and P. The degree of element segregation is defined as the difference in content between GB and matrix. The magnitudes of Cr depletion and Si enrichment at the GB_{A1} are 5.7 at.% and 2.5 at.%, respectively. The magnitude of P enrichment at the GB_{A1} is 1.5 at.% (Fig. 7g) and the P content significantly decreases from the pristine GB to the oxide tip (Fig.7e–g). P enrichment was not detected in the intergranular oxides of GB_{A1} (Fig. 7b–d), suggesting that P has directly dissolved into water. S was not counted here because

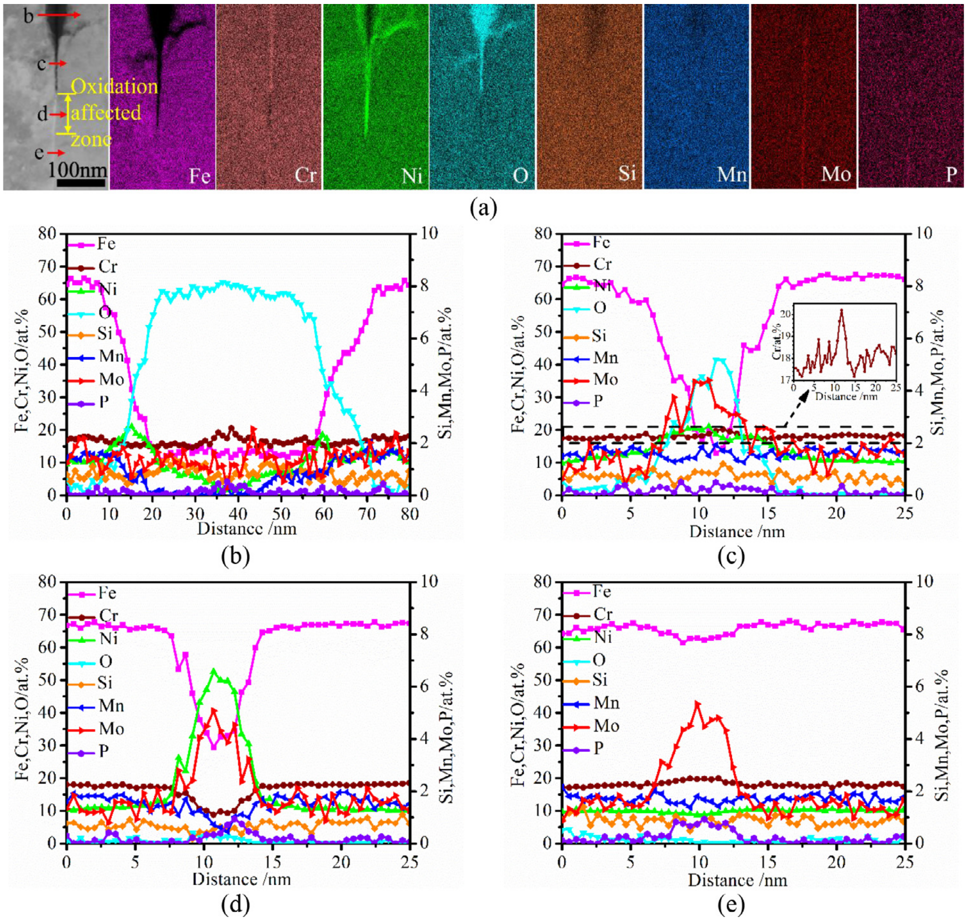

Fig. 8. (a) STEM-HAADF image and EDS mappings of the enlarged intergranular oxide tip of GB_{A2} (shown in Fig. 4b with red dotted line) in NIR and (b–e) EDS line profiles along the lines in (a).

its content is very low and the signal peak overlaps with that of Mo.

The EDS line profiles across the intergranular oxide along GB_{A2} are presented in Fig. 8b and c. As shown in Fig. 8c, the Si content in the intergranular oxide tip of GB_{A2} is 1.2 at.%, which is comparable to that in the matrix and doesn't show much variation along the GB. It should be noted that the Si content in the intergranular oxide tip of GB_{A1} is much higher than that for GB_{A2} (7.4 at.% vs. 1.2 at.%). The composition profiles of Si across the intergranular oxide of GB_{A1} show an inverted "V" shape (Fig. 7c). Considering the notable enrichment of Si at the intergranular oxide tip of GB_{A1} and the disappearance of Si enrichment just beyond the oxide tip, it is believed that Si can diffuse rapidly to the oxidation front along GB and gets oxidized. A similar phenomenon seems to apply to P at GB_{A1} except that P enrichment was not detected in the intergranular oxide (Fig. 7a-d). For GB_{A2}, intergranular oxidation also caused element segregation just beyond the intergranular oxide. It results in depletion of Fe, Cr, and enrichment of Ni. The OAZ is around 94 nm long and 5 nm wide beyond the intergranular oxide (Fig. 8a and d). The chemical composition of pristine GB in NIR is significantly different from that in UDR. Unexpectedly, Mo enrichment was observed at GB_{A2} (4.0 at.% in magnitude) (Fig. 8e), while none was detected at GB_{A1} (Fig. 7g). Mo enrichment occurred at the GBs of the as-received sample prior to proton irradiation (Fig. 8a). This phenomenon has also been found in our previous study [40]. The Mo content in the OAZ of GB_{A2} is comparable with that in the pristine segment (5.1 at.% vs. 5.3 at.%) (Fig. 8d and e), suggesting that there should be no migration of Mo element along GB during intergranular oxidation. However, Mo segregation was not observed at intergranular oxide of GB_{A2} except that at the oxide tip. It appears that Mo has dissolved into water near the sample surface. It should be noted that Mo enrichment was only observed at GB_{A2} and GB_{C2} while none was detected at GB_{B2}. According to the microchemical results, the intergranular oxidation of GB_A, GB_B and GB_C have consistent features, indicating that Mo at GB does not change the intergranular oxidation behavior. This may be related to the lowest oxidation tendency of Mo among Fe, Cr, Ni, Si, Mn, P, and Mo [45]. The magnitude of P enrichment at the GB_{A2} is 0.8 at.% (Fig. 8e). Thus, radiation induces depletion of Mo and further enrichment of P from the original state. Unlike in irradiated GB_{A1}, the P content in the OAZ is barely changed compared to the pristine GB_{A2} (Fig. 8d and e). The P element in the intergranular oxide of GB_{A2} has also dissolved into water (Fig. 8b and c). Fig. 9a and b show the STEM-HAADF images and EDS mappings of the enlarged intergranular oxide tips of GB_{B1} and GB_{B2}, respectively. From the STEM-HAADF images of cross section, there are two much wider OAZs beyond the intergranular oxides. These two OAZs show the characteristics of diffusion-induced grain boundary migration (DIGM). The original grain boundaries are marked with dashed yellow lines and the migrated boundaries are represented by broken black lines. The EDS mappings confirm that these two DIGM zones are enriched in Ni and depleted in Cr and Fe. A notable Si enrichment was also observed at the intergranular oxide tip of GB_{B1} (Fig. 9a) along the migrated GB rather than the original GB. The sizes of DIGM zone in GB_{B1} (Fig. 9a) are much larger than that in GB_{B2} (Fig. 9b). The features of intergranular oxide, oxidation affected zone (OAZ), and pristine GB in UDR and NIR are summarized in Table 3. In summary, these three pairs of GBs consistently

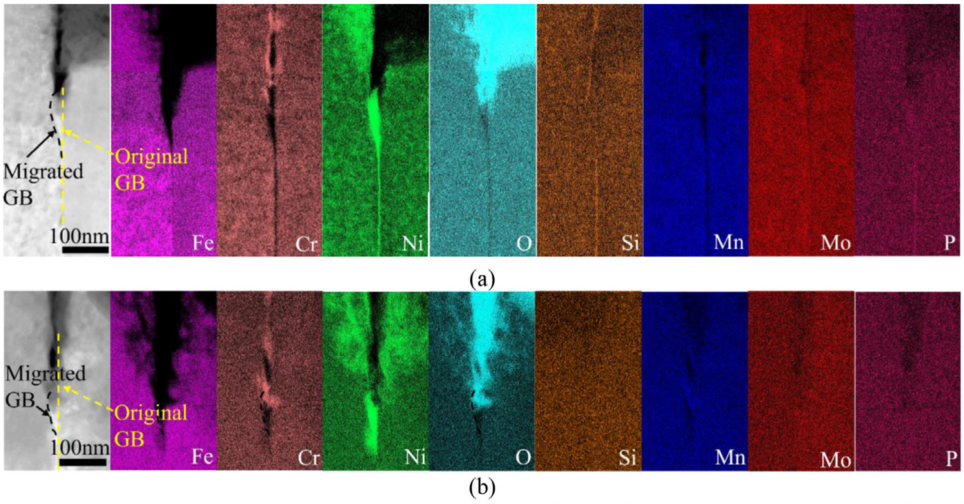

Fig. 9. STEM-HAADF images and EDS mappings of the enlarged intergranular oxide tips of (a) GB_{B1} in UDR and (b) GB_{B2} in NIR.

Table 3
Features of intergranular oxide tip, oxidation affected zone (OAZ) and pristine GB in UDR and NIR.

Features		Intergranular oxide tip	OAZ*	Pristine GB
Similarities		Enriched in Cr; Depleted in Fe and Ni; Depleted in Mn and P	Depleted in Fe, Cr and Mn; Enriched in Ni	Enriched in P
Differences	UDR	Cr across the oxide show an "M" shape; Si across the oxide show an inverted "V" shape; More enriched in Cr	Length and width in UDR are much larger than that in NIR	Depleted in Fe, Cr and Mn; Enriched in Ni and Si; More enriched in P
	NIR	Cr across the oxide show an inverted "V" shape; No Si enrichment	Occasionally enriched in Mo; Slightly enriched in P	Occasionally enriched in Mo

* Oxidation affected zone (OAZ) beyond the intergranular oxide.

show shallower intergranular oxidation depths in the irradiated region than in the unirradiated one.

The intergranular oxidation depths from the irradiated and unirradiated regions were measured from the BSE images obtained from the cross-section sample. Fig. 10a shows some of the oxidized GBs from irradiated and unirradiated regions. Fig. 10b shows the bar charts of measured intergranular oxidation depths from the irradiated and unirradiated regions. The average depths of intergranular oxidation in irradiated and unirradiated regions are 428 ± 17 nm and 537 ± 19 nm, respectively. The difference in intergranular oxidation depth obtained from BSE images between UDR and NIR is 25%, which is quite consistent with that observed from the previous sampled GBs, confirming that the resistance to intergranular oxidation after long-term immersion can be enhanced by irradiation.

4. Discussion

Surprisingly, the results presented here indicate that proton irradiation retards the intergranular oxidation after long-term immersion, which is opposite to the conclusion achieved in previous relevant work [28,29,34]. Unlike in the previous work, the effect of irradiation on oxidation was determined from the direct comparison between irradiated and un-irradiated regions of the same grain boundaries in this work. Thus, the influence due to the difference in GB structure can be eliminated. The inhibition effect of proton irradiation on intergranular oxidation will be discussed from the microchemical features of the formed oxide and the enhanced diffusivity of solute atoms along GB.

4.1. Effect of irradiation on the microchemistry of intergranular oxide

The STEM-HAADF images, EDS mappings, and line profiles shown in Figs. 3 and 6–8 reveal differences in the microchemistry of intergranular oxide of the same GB between UDR and NIR. A remarkable Si enrichment was observed at the intergranular oxide tip in UDR which was not detected in NIR. The oxide along GB in UDR is more enriched in Cr in spite of radiation-induced Cr depletion in pristine GB. According to the Ellingham-Richardson diagram, the affinity to oxygen for the relevant element is as follows: Si>Mn>Cr>Fe>Ni [45,46]. In addition, Si has the largest diffusion coefficient in austenitic alloys among these elements ($D_{Si}>D_{Cr}>D_{Ni}$) [47,48]. Therefore, Si segregated at the irradiated GB can diffuse outwards preferentially and get oxidized at

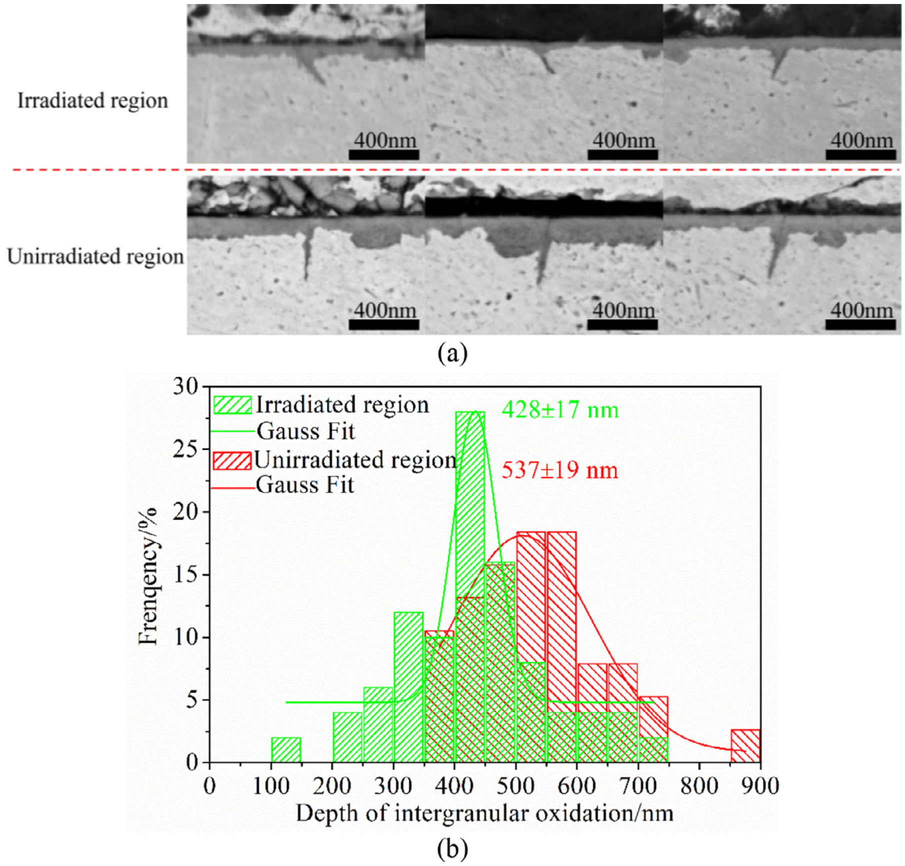

Fig. 10. (a) BSE images of cross-sectioned specimen showing some of the oxidized GBs from irradiated and unirradiated regions, (b) bar charts of measured intergranular oxidation depths from the irradiated and unirradiated regions.

the intergranular oxide tip [49]. The Si-enriched oxide can serve as a protective barrier layer in high temperature gaseous environment, but tends to dissolve in high temperature water [33,49,50]. Therefore, with the increase of intergranular oxidation depth, the Si-enriched oxide near the sample surface gradually dissolved into high temperature water. A small amount of Si-enriched oxide remains at the intergranular oxide tip due to inadequate exposure to high temperature water. Finally, Si-enriched oxide about 206 nm long is formed at the intergranular oxide tip of GB_{A1} after 1000 h immersion experiment (shown in Fig. 6a) and the Si content decreases significantly when moving from the oxide tip to the sample surface (shown in Fig. 7b–d). The undissolved Si-enriched oxide at the intergranular oxide tip can still act as a diffusion barrier and mitigate further intergranular oxidation in high temperature water. Meanwhile, as will be discussed in the next section, the transport of Cr element to the reaction front is enhanced by irradiation and Cr-enriched intergranular oxide forms. As a result, although GB_{A1} is depleted in Cr due to RIS, the maximum Cr content in the intergranular oxide tip of GB_{A1} is much higher than that of GB_{A2} (28.0 at.% vs. 20.2 at.%) (Figs. 7d and 8c). Since the Si-enriched oxide formed preferentially along the original GB and the Cr-enriched oxides developed thereafter at both sides of the original GB, the composition profiles of Si and Cr across the intergranular oxide of GB_{A1} show an inverted “V” shape and an “M” shape (Fig. 7c), respectively. Given that these two types of oxides are complementarily distributed in intergranular oxide (shown in Fig. 7c), it is believed that both oxides should contribute to the improved resistance to intergranular oxidation. As the volume of Cr-rich oxide at the intergranular oxide tip is much larger than that of Si-rich oxide, the Cr-rich oxide may play a greater role in improving the resistance to oxidation of irradiated GB. In contrast, as there is no Si enrichment in the un-irradiated GB, the composition profile of Cr across the intergranular oxide of GB_{A2} shows an inverted “V” shape with no Si enrichment in the oxide (Fig. 8c). In summary, the elevated Cr content in combination with Si enrichment in the intergranular oxide tip can enhance the resistance to intergranular oxidation when the sample is not stressed and eventually leads to a lower oxidation rate for the irradiated GB.

4.2. Effect of irradiation on solute diffusivity along grain boundary

As discussed above, the mixture of Cr and Si enriched oxides at the intergranular oxide tip can act as a temporary protective barrier and result in a lower oxidation rate at irradiated GB_{A1}. The kinetic factor should also be taken into account to explain the suppressed intergranular oxidation along irradiated GB, i.e., enhanced solute diffusivity by irradiation. The enhanced solute diffusivity by irradiation can be verified by the fact that the size of OAZ (quantified by length and width) beyond the intergranular oxide is much larger in GB_{A1} than that in GB_{A2}, as shown in Figs. 7a and 8a. Due to the outward diffusion of Si and Cr beyond the intergranular oxide tip, the local composition is remarkably affected. Ni was further enriched while Cr was further depleted in addition to RIS beyond the intergranular oxide tip of GB_{A1} and the OAZ is around 250 nm long and 15 nm wide (Fig. 7a and e). In comparison, the OAZ extends only about 94 nm long and 5 nm wide beyond the intergranular oxide tip of GB_{A2} (Fig. 8a and d). It should be noted that the widths of OAZ beyond the intergranular oxide of GB_B are much larger than those of GB_A, and it is easier to identify the diffusion-induced grain boundary migration (DIGM) zone (Fig. 9). Anyway, the sizes of OAZ in UDR are always larger than those in NIR for all the sampled GBs, as listed in Table 4. Meanwhile, the maximum Cr

Table 4
Sizes of oxidation affected zone (OAZ), maximum Cr content in intergranular oxide and intergranular oxide penetration of GB_A, GB_B and GB_C, respectively.

GB		OAZ* (nm)		Max. Cr content**(at. %)	Intergranular oxide penetration(nm)
		Length	Width		
GB_A	GB_{A1}	250	15	28.0	427
	GB_{A2}	94	5	20.0	575
GB_B	GB_{B1}	150	25	34.0	490
	GB_{B2}	92	13	23.7	618
GB_C	GB_{C1}	169	18	30.2	515
	GB_{C2}	0	0	21.5	604

* Oxidation affected zone (OAZ) beyond the intergranular oxide.

** The maximum Cr content in the intergranular oxide.

content at the intergranular oxide tip of GB in UDR is much higher than that of GB in NIR. Therefore, the efficiency of element (especially Cr) transport along GB has been promoted by irradiation.

It should be noted that the only diffusion path for Cr to the oxidation front is through GB which then migrates. The migration of GB is accompanied by the diffusion of Cr from the first few monolayers of one grain near the new migrated GB. Thus, the amount of diffused Cr can be measured by the size of the DIGM (or OAZ) zone. It should be noted that vacancy is the dominant carrier for diffusion because the concentration of interstitial is much lower than that of vacancy after the irradiation. As discussed above, Si segregated at the irradiated GB can diffuse outwards preferentially due to its high diffusivity and leaves behind many vacancies which can promote the diffusion of other solute atoms. The diffusivity of lattice atoms by vacancy mechanism is given by: $D = f_v D_v C_v$, where D_v is the vacancy diffusion coefficient, C_v is the vacancy concentration and f_v is the correlation coefficient. Thus, increased vacancy concentration can increase the diffusion coefficient of atoms. It is believed that the situation is similar for diffusion at GB as vacancy is also the major participant in the process of GB diffusion [51]. That is, vacancies produced by preferential diffusion of Si beyond the oxide tip at irradiated GB can enhance the diffusion of other slow-moving elements like Cr. This forms a concentration gradient of Cr between matrix (one grain near the migrated GB) and GB which further drives its diffusion to GB. That is why the intergranular oxide tip contains higher content of Cr in UDR than in NIR even when Cr is already depleted in UDR due to RIS. Diffusivity of P was also promoted in UDR as remarkable depletion of P occurred in the OAZ of irradiated GB while significant P could still be detected in the OAZ of un-irradiated GB although P segregated at GB after irradiation (Figs.7 and 8). Similarly, it has been reported that a high entropy alloy (HEA) (28%Fe-27%Ni-27%Mn-18%Cr) can form a Cr-rich oxide film over GB in 320 °C hydrogenated water [52] while austenitic stainless steel containing a similar amount of Cr is normally susceptible to intergranular oxidation. That is because Cr diffusion along grain boundary in the HEA was promoted due to the fast diffusion of Mn. Irradiation induced defects may also affect elements diffusion along the grain boundary. It is believed that vacancies or voids should have little effect on the diffusivity along grain boundary as there is a denuded zone adjacent to the grain boundary [53,54]. Nevertheless, dislocation loops were observed near the grain boundary which can facilitate the diffusion of elements like Cr.

The enhanced diffusivity of Cr along irradiated GB helps to mitigate the intergranular oxidation to some extent. Some previous works also suggest that the efficiency of Cr transport is vital to the resistance to corrosion. Zhou et al. [55] reported that *in-situ* proton irradiation enhances the diffusion of Cr and Ni from matrix to GBs and compensates the dissolution of Cr from GB to molten salt, which eventually decelerates the intergranular corrosion of Ni-Cr alloys. Similar effect was also found in general corrosion. Hanbury and Was [12] reported that *in-situ* proton irradiation promoted diffusion of Cr element and resulted in a decrease of inner oxide thickness of stainless steels in 320 °C hydrogenated water. Thus, the diffusivity of Cr is vital to the resistance to corrosion. Furthermore, the effect of Cr diffusivity on the protectiveness of oxide would be eventually linked to the SCC resistance. He et al. [56] found that the efficiency of Cr transport along GB is closely related to the site-specific susceptibility to SCC of a Fe-13Cr-15Ni alloy in simulated boiling water reactor normal water. Kuang et al. [25,57] demonstrated that the efficiency of Cr diffusion along GB in alloy 690 dictates the ability to form a compact chromia film over the GB in high temperature hydrogenated water, and also the compactness of oxide beyond the crack tip. Therefore, the diffusivity of Cr is an important factor affecting the corrosion and SCC resistance of material.

4.3. Relevance of intergranular oxidation to SCC

It should be noted that the exposed sample was not stressed during the test. The current results indicate that the Si-enriched oxide formed at the intergranular oxide tip in UDR can serve as a temporary protective barrier and retard the inward diffusion of oxygen along the GB. It is quite unexpected since the previous studies suggested that elevated bulk Si content promotes SCC growth rate in simulated PWR primary water [49,58]. Moreover, Kuang et al. [33] found that the decreasing SCC growth rate of neutron-irradiated 304L stainless steel in reducing high temperature water was correlated with the reduced GB Si content which was achieved through annealing treatments. Such inconsistency should result from the stress condition. It has been reported that the adhesion of oxide decreases with addition of Si into the stainless steel [59,60]. The brittle character of the silica formed on stainless steel is often considered as the primary cause of oxide scale spallation [59,60]. Similarly, it is believed that Si-enriched oxide formed at the intergranular oxide tip in UDR would degrade the strength of GB and can be easily breached under stress. The Si-enriched oxide would dissolve in solution quickly once the crack initiates, hence accelerating the crack propagation. Indeed, the length and maximum Si content of Si-enriched oxide at intergranular oxide tip in UDR in this work (206 nm, 7.4 at.%) are much larger than those beyond an IASCC crack from the same material which has been reported in our previous work (~50 nm, 3.2 at.%) [40]. Thus, the SCC susceptibility depends not only on the degree of intergranular oxidation but also on the property of the formed oxide.

Fig. 11 depicts the process of intergranular oxidation for the irradiated GB and its un-irradiated counterpart. For the irradiated GB (Fig. 11a), Si segregated at the GB can diffuse outwards preferentially and get oxidized at the intergranular oxide tip due to its high diffusivity and affinity to oxygen. The fast diffusion of Si creates vacancies which enhance the diffusion of Cr to the oxida-

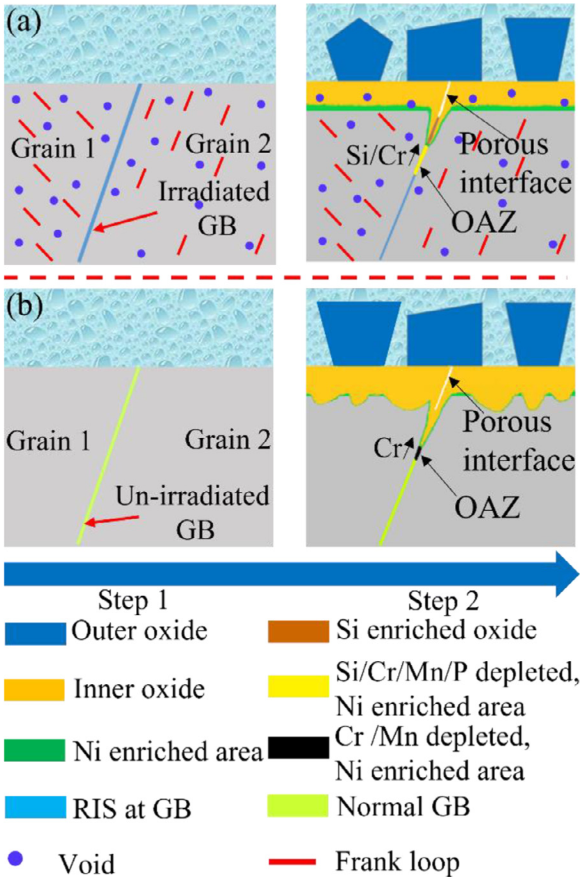

Fig. 11. Schematic of intergranular oxidation behavior for the (a) irradiated GB and its (b) un-irradiated counterpart.

tion front. Hence, the oxide along irradiated GB is more enriched in Cr in spite of Cr depletion induced by RIS at pristine GB. The combination of Si and Cr enrichments in the intergranular oxide tip leads to a lower oxidation rate in irradiated GB than in un-irradiated GB (Fig. 11b). In addition, the OAZ formed beyond the intergranular oxide tip of irradiated GB is much larger than that of un-irradiated GB (Fig. 11a and b) due to the enhanced diffusion of solute atoms (especially Cr) along the irradiated GB. This work demonstrates that it is crucial to eliminate the interference from the difference in GB structure when studying the irradiation effect on intergranular oxidation. By doing so, the mitigation of intergranular oxidation by irradiation was determined here for the first time. The mitigating effect of irradiation on intergranular oxidation is in contrast to the irradiation-assisted SCC, indicating that the property of formed oxide is also important to SCC resistance. Furthermore, the mitigation of intergranular oxidation by irradiation may be influenced by the irradiation dose and oxidation time which necessitates further detailed study.

5. Conclusions

The effect of proton irradiation on the intergranular oxidation of 316L stainless steel after exposure to simulated PWR primary water for 1000 h was clarified by ruling out the interference from the difference in GB structure. The following conclusions can be drawn in this study.

(1) The intergranular oxide penetration in non-irradiated region (NIR) is deeper than that in uniformly-damaged region (UDR), indicating that proton irradiation has a mitigation effect on intergranular oxidation after long-term immersion.
(2) Due to its high diffusivity and affinity to oxygen, Si enriched in UDR due to radiation-induced segregation (RIS) diffuses out preferentially and promotes the formation of Si-enriched oxide at the intergranular oxide tip. The Si-enriched oxide at the intergranular oxide tip can act as a temporary diffusion barrier for oxygen although it tends to dissolve into high temperature water near the sample surface.
(3) The efficiency of elements (especially Cr) transport along grain boundary to oxidation front is promoted in UDR mainly due to vacancies created by the preferential diffusion of Si, resulting in a larger oxidation affected zone (OAZ) beyond the intergranular oxide tip. Meanwhile, the maximum Cr content at the intergranular oxide tip in UDR is much higher than that in NIR.
(4) The elevated Cr content in combination with Si enrichment in the intergranular oxide in UDR can enhance the resistance to intergranular oxidation when the sample is not stressed, eventually leading to a lower intergranular oxidation rate in UDR compared in NIR.

Declaration of Competing Interest

The authors declare that they have no known competing financial interests or personal relationships that could have appeared to influence the work reported in this paper.

Acknowledgements

The authors gratefully acknowledge the financial support of National Natural Science Foundation of China (No. 51971172) and the Young Talent Support Plan of Xi'an Jiaotong University. The authors thank Dr. Jiao Li at Instrument Analysis Center of Xi'an Jiaotong University for her assistance with STEM and EDS analysis. The authors also thank Prof. Genshu Zhou and Dr. Shaojun Wu at Xi'an Jiaotong University for their assistance in Ni plating, and research fellow Wei Wang for his assistance in SEM characterization.

References

[1] Z. Jiao, G.S. Was, Localized deformation and IASCC initiation in austenitic stainless steels, J. Nucl. Mater. 382 (2008) 203–209.
[2] K.F.H. Nishioka, K. Fujii, T. Torimaru, IASCC initiation in highly irradiated stainless steels under uniaxial constant load conditions, J. Nucl. Sci. Technol. 45 (2008) 1072–1077.
[3] Y. Chen, B. Alexandreanu, W.K. Soppet, W.J. Shack, K. Natesan, A.S. Rao, Slow strain rate tensile tests of irradiated austenitic stainless steels in simulated PWR environment, in: Proceedings of the 15th International Conference on Environmental Degradation of Materials in Nuclear Power Systems-Water Reactors, Colorado Springs, Colorado, USA, 2011.
[4] D. Du, K. Sun, G.S. Was, IASCC of neutron irradiated 316 stainless steel to 125 dpa, Mater. Charact. 173 (2021) 110897.
[5] K.J. Stephenson, G.S. Was, Crack initiation behavior of neutron irradiated model and commercial stainless steels in high temperature water, J. Nucl. Mater. 444 (2014) 331–341.
[6] K. Fukuya, M. Nakano, K. Fujii, T. Torimaru, IASCC susceptibility and slow tensile properties of highly-irradiated 316 stainless steels, J. Nucl. Sci. Technol. 41 (2004) 673–681.
[7] M.D. Mcmurtrey, G.S. Was, Role of slip behavior in the irradiation assisted stress corrosion cracking in austenitic steels, in: Proceedings of the 15th International Conference on Environmental Degradation of Materials in Nuclear Power Systems-Water Reactors, Colorado Springs, Colorado, USA, 2011.
[8] G.P. Marsh, K.J. Taylor, G. Bryan, S.E. Worthington, The influence of radiation on the corrosion of stainless steel, Corros. Sci. 26 (1986) 971–982.
[9] B. Pastina, J.A. LaVerne, Hydrogen peroxide production in the radiolysis of water with heavy ions, J. Phys. Chem. A. 103 (1999) 1592–1597.
[10] S.S. Raiman, G.S. Was, Accelerated corrosion and oxide dissolution in 316L stainless steel irradiated *in situ* in high temperature water, J. Nucl. Mater. 493 (2017) 207–218.
[11] S.S. Raiman, D.M. Bartels, G.S. Was, Radiolysis driven changes to oxide stability during irradiation-corrosion of 316L stainless steel in high temperature water, J. Nucl. Mater. 493 (2017) 40–52.
[12] R.D. Hanbury, G.S. Was, Oxide growth and dissolution on 316L stainless steel during irradiation in high temperature water, Corros. Sci. 157 (2019) 305–311.
[13] K. Stephenson, G.S. Was, The role of dislocation channeling in IASCC initiation of neutron irradiated stainless steel, J. Nucl. Mater. 481 (2016) 214–225.

[14] G.S. Was, J.T. Busby, Role of irradiated microstructure and microchemistry in irradiation-assisted stress corrosion cracking, Philos. Mag. 85 (2005) 443–465.
[15] M.D. McMurtrey, B. Cui, I. Robertson, D. Farkas, G.S. Was, Mechanism of dislocation channel-induced irradiation assisted stress corrosion crack initiation in austenitic stainless steel, Curr. Opin. Solid State Mater. Sci. 19 (2015) 305–314.
[16] H. Nishioka, K. Fukuya, K. Fujji, Y. Kitsunai, Deformation structure in highly irradiated stainless steels, J. Nucl. Sci. Technol. 45 (2008) 274–287.
[17] Z. Jiao, G.S. Was, Impact of localized deformation on IASCC in austenitic stainless steels, J. Nucl. Mater. 408 (2011) 246–256.
[18] D. Du, K. Sun, G.S. Was, Crack initiation of neutron-irradiated 304L stainless steel in PWR primary water, Corros. Sci. 193 (2021) 109902.
[19] J. Panter, B. Viguier, J.M. Cloué, M. Foucault, P. Combrade, E. Andrieu, Influence of oxide films on primary water stress corrosion cracking initiation of alloy 600, J. Nucl. Mater. 348 (2006) 213–221.
[20] P.M. Scott, An overview of internal oxidation as a possible explanation of intergranular stress corrosion cracking of alloy 600 in PWRS, in: Proceedings of the Ninth International Symposium on Environmental Degradation of Materials in Nuclear Power Systems-Water Reactors, Newport Beach, USA, 1999.
[21] P.L. Andresen, F.P. Ford, Life prediction by mechanistic modeling and system monitoring of environmental cracking of iron and nickel alloys in aqueous systems, Mater. Sci. Eng. A 103 (1988) 167–184.
[22] P.L. Andresen, Fracture mechanics data and modeling of environmental cracking of nickel-base alloys in high-temperature water, Corrosion 47 (1991) 917–938.
[23] M. Meisnar, A. Vilalta-Clemente, M. Moody, K. Arioka, S. Lozano-Perez, A mechanistic study of the temperature dependence of the stress corrosion crack growth rate in SUS316 stainless steels exposed to PWR primary water, Acta Mater. 114 (2016) 15–24.
[24] Y.Z. Huang, J.M. Titchmarsh, TEM investigation of intergranular stress corrosion cracking for 316 stainless steel in PWR environment, Acta Mater. 54 (2006) 635–641.
[25] W. Kuang, M. Song, G.S. Was, Insights into the stress corrosion cracking of solution annealed alloy 690 in simulated pressurized water reactor primary water under dynamic straining, Acta Mater. 151 (2018) 321–333.
[26] W. Kuang, G.S. Was, A high-resolution characterization of the initiation of stress corrosion crack in Alloy 690 in simulated pressurized water reactor primary water, Corros. Sci. 163 (2020) 108243.
[27] P.M. Scott, P. Combrade, General corrosion and stress corrosion cracking of Alloy 600 in light water reactor primary coolants, J. Nucl. Mater. 524 (2019) 340–375.
[28] P. Deng, Q. Peng, E.H. Han, W. Ke, C. Sun, Z. Jiao, Effect of irradiation on corrosion of 304 nuclear grade stainless steel in simulated PWR primary water, Corros. Sci. 127 (2017) 91–100.
[29] M. Boisson, L. Legras, E. Andrieu, L. Laffont, Role of irradiation and irradiation defects on the oxidation first stages of a 316L austenitic stainless steel, Corros. Sci 161 (2019) 108194.
[30] Z. Jiao, G. Was, Oxidation of a proton-irradiated 316 stainless steel in simulated BWR NWC environment, in: Proceedings of the 15th International Conference on Environmental Degradation of Materials in Nuclear Power Systems-Water Reactors, Colorado Springs, Colorado, USA, 2011.
[31] S. Perrin, L. Marchetti, C. Duhamel, M. Sennour, F. Jomard, Influence of irradiation on the oxide film formed on 316L stainless steel in PWR primary water, Oxid. Metal 80 (2013) 623–633.
[32] S.M. Bruemmer, E.P. Simonen, P.M. Scott, P.L. Andresen, G.S. Was, J.L. Nelson, Radiation-induced material changes and susceptibility to intergranular failure of light-water-reactor core internals, J. Nucl. Mater. 274 (1999) 299–314.
[33] W. Kuang, J. Hesterberg, G.S. Was, The effect of post-irradiation annealing on the stress corrosion crack growth rate of neutron-irradiated 304L stainless steel in boiling water reactor environment, Corros. Sci. 161 (2019) 108183.
[34] T. Fukumura, K. Fukuya, K. Fujii, T. Miura, Y. Kitsunai, Grain Boundary Oxidation of Neutron Irradiated Stainless Steels in Simulated PWR Water, in: Proceedings of the 18th International Conference on Environmental Degradation of Materials in Nuclear Power Systems-Water Reactors, Portland, Oregon, USA, Marriott Portland Downtown Waterfront, 2017.
[35] C.M. Barr, G.A. Vetterick, K.A. Unocic, K. Hattar, X.M. Bai, M.L. Taheri, Anisotropic radiation-induced segregation in 316L austenitic stainless steel with grain boundary character, Acta Mater. 67 (2014) 145–155.
[36] S. Watanabe, Y. Takamatsu, N. Sakaguchi, H. Takahashi, Sink effect of grain boundary on radiation-induced segregation in austenitic stainless steel, J. Nucl. Mater. 283–287 (2000) 152–156.
[37] Y.S. Lim, S.W. Kim, S.S. Hwang, H.P. Kim, C. Jang, Intergranular oxidation of Ni-based Alloy 600 in a simulated PWR primary water environment, Corros. Sci. 108 (2016) 125–133.
[38] G.S. Was, J.T. Busby, T. Allen, E.A. Kenik, A. Jensson, S.M. Bruemmer, J. Gan, A.D. Edwards, P.M. Scott, P.L. Andreson, Emulation of neutron irradiation effects with protons: validation of principle, J. Nucl. Mater. 300 (2002) 198–216.
[39] R.E. Stoller, M.B. Toloczko, G.S. Was, A.G. Certain, S. Dwaraknath, F.A. Garner, On the use of SRIM for computing radiation damage exposure, Nucl. Instrum. Methods Phys. Res. Sect. B 310 (2013) 75–80.
[40] W. Kuang, X. Feng, D. Du, M. Song, M. Wang, G.S. Was, A high-resolution characterization of irradiation-assisted stress corrosion cracking of proton-irradiated 316L stainless steel in simulated pressurized water reactor primary water, Corros. Sci. 199 (2022) 110187.
[41] X. Feng, J. Xie, W. Kuang, A novel approach to index site-specific grain boundary plane, Mater. Charact. 174 (2021) 110999.
[42] W. Kuang, G.S. Was, The effect of grain boundary structure on the intergranular degradation behavior of solution annealed alloy 690 in high temperature, hydrogenated water, Acta Mater. 182 (2020) 120–130.
[43] S. Lozano-Perez, K. Kruska, I. Iyengar, T. Terachi, T. Yamada, The role of cold work and applied stress on surface oxidation of 304 stainless steel, Corros. Sci. 56 (2012) 78–85.
[44] L. Legras, B. Marylou, F. Elodie, C. Priscille, M. Remi, M. Salem, T. Jinane, R. Menand, TEM Investigations of the Microstructure and Oxides at the Tip of Intergranular Cracks of a Baffle Former Bolt Irradiated up to 10 dpa, FONTEVRAUD 9, Avignon, France, 2018.
[45] C.V. Robino, Representation of mixed reactive gases on free energy (Ellingharn-Richardson) diagrams, Metall. Mater. Trans. B 27 (1996) 65–69.
[46] Z. Zhang, E.H. Han, C. Xiang, Effect of helium ion irradiation on short-time corrosion behavior of two novel high-entropy alloys in simulated PWR primary water, Corros. Sci. 191 (2021) 109742.
[47] P.R. Okamoto, L.E. Rehn, Radiation-induced segregation in binary and ternary alloys, J. Nucl. Mater. 83 (1979) 2–23.
[48] J.T. Busby, G.S. Was, E.A. Kenik, Isolating the effect of radiation-induced segregation in irradiation-assisted stress corrosion cracking of austenitic stainless steels, J. Nucl. Mater. 302 (2002) 20–40.
[49] P.L. Andresen, M.M. Morra, Effects of Si on SCC of irradiated and unirradiated stainless steel and nickel alloys, in: Proceedings of the 12th International Conference on Environmental Degradation of Materials in Nuclear Power Systems: Water Reactors, Salt Lake City, Utah, USA, 2005.
[50] R.O. Fournier, J.J. Rowe, The solubility of amorphous silica in water at high temperatures and high pressures, Am. Mineral. 62 (9–10) (1977) 1052–1056.
[51] A. Suzuki, Y. Mishin, Atomic mechanisms of grain boundary diffusion: Low versus high temperatures, J. Mater. Sci. 40 (2005) 3155–3161.
[52] J. Dong, X. Feng, X. Hao, W. Kuang, The environmental degradation behavior of FeNiMnCr high entropy alloy in high temperature hydrogenated water, Scr. Mater. 204 (2021) 114127.
[53] B.N. Singh, S.J. Zinkle, Influence of irradiation parameters on damage accumulation in metals and alloys, J. Nucl. Mater. 217 (1994) 161–171.
[54] Y. Sekio, S. Yamashita, N. Sakaguchi, H. Takahashi, Void denuded zone formation for Fe–15Cr–15Ni steel and PNC316 stainless steel under neutron and electron irradiations, J. Nucl. Mater. 458 (2014) 355–360.
[55] W. Zhou, Y. Yang, G. Zheng, K.B. Woller, P.W. Stahle, A.M. Minor, M.P. Short, Proton irradiation-decelerated intergranular corrosion of Ni-Cr alloys in molten salt, Nat. Commun. 11 (2020) 3430.
[56] M.R. He, D.C. Johnson, G.S. Was, I.M. Robertson, The role of grain boundary microchemistry in irradiation-assisted stress corrosion cracking of a Fe-13Cr-15Ni alloy, Acta Mater. 138 (2017) 61–71.
[57] W. Kuang, G.S. Was, The effect of grain boundary structure on the intergranular degradation behavior of solution annealed Alloy 690 in high temperature, hydrogenated water, Acta Mater. 182 (2020) 120–130.
[58] G.F. Li, Y. Kaneshima, T. Shoji, Effects of impurities on environmentally assisted crack growth of solution-annealed austenitic steels in primary water at 325°C, Corrosion 56 (2000) 460–469.
[59] H.E. Evans, D.A. Hilton, R.A. Holm, S.J. Webster, Influence of silicon additions on the oxidation resistance of a stainless steel, Oxid. Metal 19 (1983) 1–18.
[60] G. Bamba, Y. Wouters, A. Galerie, F. Charlot, A. Dellali, Thermal oxidation kinetics and oxide scale adhesion of Fe–15Cr alloys as a function of their silicon content, Acta Mater. 54 (2006) 3917–3922.